

Laser Activation for Highly Boron-Doped Passivated Contacts

Saman Sharbaf Kalaghichi ^{1,2,*}, Jan Hoß ¹, Renate Zapf-Gottwick ² and Jürgen H. Werner ²

¹ International Solar Energy Research Center Konstanz, Rudolf-Diesel-Straße 15, 78467 Konstanz, Germany; jan.hoss@isc-konstanz.de

² Institute for Photovoltaics, University of Stuttgart, Pfaffenwaldring 47, 70569 Stuttgart, Germany; rena.te.zapf-gottwick@ipv.uni-stuttgart.de (R.Z.-G.); juergen.werner@ipv.uni-stuttgart.de (J.H.W.)

* Correspondence: saman.sharbaf@isc-konstanz.de

Abstract: Passivated, selective contacts in silicon solar cells consist of a double layer of highly doped polycrystalline silicon (poly Si) and thin interfacial silicon dioxide (SiO₂). This design concept allows for the highest efficiencies. Here, we report on a selective laser activation process, resulting in highly doped p⁺⁺-type poly Si on top of the SiO₂. In this double-layer structure, the p⁺⁺-poly Si layer serves as a layer for transporting the generated holes from the bulk to a metal contact and, therefore, needs to be highly conductive for holes. High boron-doping of the poly Si layers is one approach to establish the desired high conductivity. In a laser activation step, a laser pulse melts the poly Si layer, and subsequent rapid cooling of the Si melt enables electrically active boron concentrations exceeding the solid solubility limit. In addition to the high conductivity, the high active boron concentration in the poly Si layer allows maskless patterning of p⁺⁺-poly Si/SiO₂ layers by providing an etch stop layer in the Si etchant solution, which results in a locally structured p⁺⁺-poly Si/SiO₂ after the etching process. The challenge in the laser activation technique is not to destroy the thin SiO₂, which necessitates fine tuning of the laser process. In order to find the optimal processing window, we test laser pulse energy densities (H_p) in a broad range of $0.7 \text{ J/cm}^2 \leq H_p \leq 5 \text{ J/cm}^2$ on poly Si layers with two different thicknesses $d_{\text{poly Si},1} = 155 \text{ nm}$ and $d_{\text{poly Si},2} = 264 \text{ nm}$. Finally, the processing window $2.8 \text{ J/cm}^2 \leq H_p \leq 4 \text{ J/cm}^2$ leads to the highest sheet conductance (G_{sh}) without destroying the SiO₂ for both poly Si layer thicknesses. For both tested poly Si layers, the majority of the symmetric lifetime samples processed using these H_p achieve a good passivation quality with a high implied open circuit voltage (iV_{OC}) and a low saturation current density (J_0). The best sample achieves $iV_{\text{OC}} = 722 \text{ mV}$ and $J_0 = 6.7 \text{ fA/cm}^2$ per side. This low surface recombination current density, together with the accompanying measurements of the doping profiles, suggests that the SiO₂ is not damaged during the laser process. We also observe that the passivation quality is independent of the tested poly Si layer thicknesses. The findings of this study show that laser-activated p⁺⁺-poly Si/SiO₂ are not only suitable for integration into advanced passivated contact solar cells, but also offer the possibility of maskless patterning of these stacks, substantially simplifying such solar cell production.



Citation: Sharbaf Kalaghichi, S.; Hoß, J.; Zapf-Gottwick, R.; Werner, J.H. Laser Activation for Highly Boron-Doped Passivated Contacts. *Solar* **2023**, *3*, 362–381. <https://doi.org/10.3390/solar3030021>

Academic Editor: Dongsheng Li

Received: 9 June 2023

Revised: 7 July 2023

Accepted: 10 July 2023

Published: 12 July 2023

Keywords: laser activation; TOPCon solar cells; passivated contact layers; poly Si doping; implied open circuit voltage; sheet conductance; carrier mobility



Copyright: © 2023 by the authors. Licensee MDPI, Basel, Switzerland. This article is an open access article distributed under the terms and conditions of the Creative Commons Attribution (CC BY) license (<https://creativecommons.org/licenses/by/4.0/>).

1. Introduction

Passivated emitter rear cells (PERC) are the current dominant technology in silicon-based photovoltaic (PV) production. The growing need for higher conversion efficiencies has encouraged the PV industry to seek alternatives to PERC design. Among the ideas for the mass production of highly efficient silicon solar cells, tunnel oxide passivated contact (TOPCon) solar cells are considered an upcoming replacement for PERC cells since only a few additional production steps are required to upgrade a PERC cell production line to a TOPCon production line [1]. The principle of the TOPCon design relies on separating the carrier extraction zone from the carrier generation zone by using a layer stack, which consists of a thin interfacial silicon dioxide layer and a highly doped polycrystalline silicon

(SiO₂/poly Si) layer [2]. The SiO₂ passivates the mono-crystalline silicon (c-Si) surface and simultaneously separates the c-Si bulk carrier generation zone from the highly doped poly Si carrier transport layer [3]. Such layer stacks result in an excellent passivation quality together with low contact resistivity.

Conventional TOPCon cells employ a highly n-type-doped poly Si layer (n⁺-poly Si), which is usually doped in ex situ furnace diffusion [?] or deposited as an in situ doped poly Si layer followed by a furnace activation step [6?]. Furnace-based processes allow for high throughput production of conventional TOPCon cells. However, these furnace processes have several inherent limitations:

- **Full area processing of poly Si layer:** Advanced passivated contact cell concepts—such as poly Si passivated interdigitated back contact (IBC) solar cells or other cells with selective poly Si passivated contacts on the front side—rely on structuring of poly Si layers, which usually requires additional complex masking steps. Such structuring steps are expensive and time-consuming; therefore, they are not favorable industrially [7,8];
- **Doping concentrations within the poly Si layer:** High doping concentrations are required within the poly Si in the poly Si/SiO₂/c-Si structure to establish low resistivity of the metal/semiconductor contact [9]. However, the doping concentration in poly Si must drop sharply at the poly Si/SiO₂ interface. Deep dopant diffusion, through the oxide into the underlying (single) crystalline silicon bulk substrate, would result in increased Auger recombination in the Si bulk [1]. The high required doping of the poly Si is particularly challenging, if one does not use n⁺-doping with phosphorus, but p⁺-doping with boron, because of the lower solid solubility of boron in silicon compared to phosphorus at the same temperature. The solid solubility of boron in Si is $s_{\max} \approx 5 \times 10^{20} \text{ cm}^{-3}$ at 1200 °C, while phosphorus has a higher solubility of $s_{\max} \approx 1.5 \times 10^{21} \text{ cm}^{-3}$ at the same temperature [10]. Elevating the boron diffusion temperature to increase the doping concentration leads to damaged SiO₂ and deep diffusion of boron into the under-laying bulk of the crystalline Si, and, consequently, to a lower passivation quality [11].

Laser irradiation—instead of furnace processing—avoids these limitations: It avoids structuring, heats the cells only locally, and, in addition, if performed properly, it also saves time. Consequently, lasers are attractive for solar cell production. For example, already, laser-doped selective emitters[12,13] and laser-doping of c-Si from precursor layers are two common production steps in the PV industry [14]. However, laser processing a poly Si/SiO₂ stack is more challenging since it requires processing a thin poly Si layer without destroying the SiO₂ underneath; the thickness of the tunneling oxide is only a few nanometers, while the laser-heated poly Si is more than a hundred times thicker.

This work presents a laser activation process for creating p⁺⁺-poly Si/SiO₂ stacks for passivated contact solar cell designs. Our laser process locally heats and melts a poly Si layer and the subsequent rapid cooling of the Si melt results in highly active boron concentrations exceeding the solid solubility limit within the poly Si layer. For our conditions, this high concentration drops sharply at the p⁺⁺-poly Si/SiO₂ interface, indicating that SiO₂ is not damaged during the laser process. As a consequence, we observe an outstanding passivation quality with a high implied open circuit voltage (iV_{OC}) and a low saturation current density (J_0). The best sample shows $iV_{OC} = 722 \text{ mV}$ and $J_0 = 6.7 \text{ fA/cm}^2$.

The high boron doping concentration also enables the maskless patterning of laser-activated p⁺⁺-poly Si/SiO₂ stacks. Buchholz et al. [15] introduced a maskless process for establishing local p⁺⁺-poly Si layers using the etch selectivity of a heavily boron-doped p⁺⁺-poly Si in the alkaline etchant. A green laser was used in their method to create high doping concentrations locally, which resulted in structured p⁺⁺-poly Si layers after etching. However, they did not show that this process could be used for highly doping the poly Si in a passivated contact solar cell design. Here, we show that this is possible. Consequently, in the next step, we will implement this approach to create local p⁺⁺-poly Si/SiO₂ stacks in advanced passivated contact solar cells.

Figure 1a shows the solar cell design with selective p^{++} -poly Si/SiO₂ stacks on the front side. To avoid parasitic optical losses by free-carrier absorption [16,17], the p^{++} -poly Si/SiO₂ passivation layers (indicated by a dashed circle) are only locally created underneath the front metal contacts.

Figure 1b illustrates the schematics of a poly Si passivated IBC solar cell. Such a solar cell design (with ion implantation and a masking process) achieved a remarkable conversion efficiency $\eta = 26.1\%$ at laboratory scale [18]. Maskless, defect-free patterning of the p^{++} -poly Si layers, as performed here, would substantially simplify the fabrication process and could open the door for the low-cost, large-scale, industrial production of this passivated contact solar cell design.

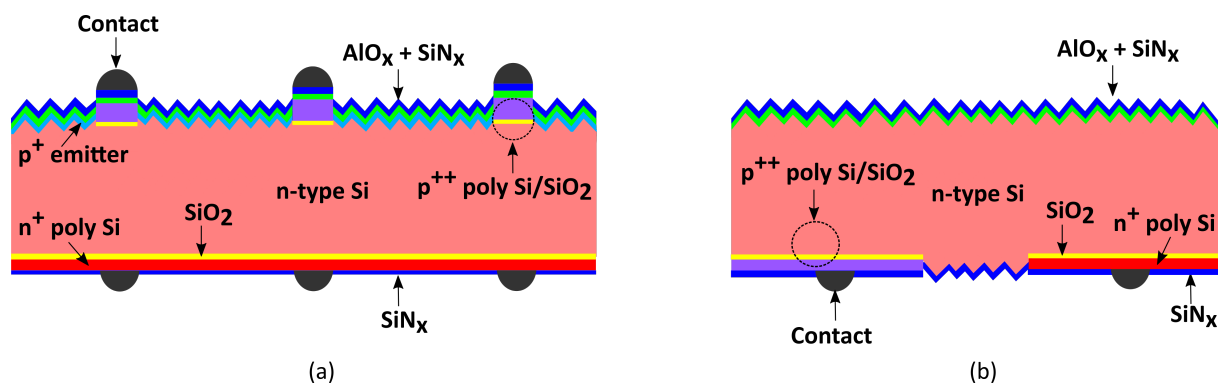


Figure 1. Schematic drawing of desired advanced passivated contact solar cells with local p^{++} poly Si/SiO₂ stacks. (a) Selective p^{++} poly Si/SiO₂ passivated front side cell. The full area n^{+} -poly Si/SiO₂ double layer passivates the rear side of the cell, while, at the front, p^{++} -poly Si/SiO₂ passivation stacks are selectively placed under the front metal contact to prevent parasitic optical losses. (b) Passivated contact, interdigitated back contact IBC solar cells. Back contacts of the cell are passivated by selectively created, laser-activated, p^{++} -poly Si/SiO₂ stack and n^{+} -poly Si/SiO₂ layers.

A laser process for dopant activation in hole-selective poly Si/SiO₂ passivation stacks has also recently been introduced by Chen et al. [19]. Their main focus was the use of gallium as an alternative p-type dopant instead of boron to overcome the passivation loss arising from boron segregation at the interface between SiO₂ and c-Si. The authors used an excimer laser for dopant activation on gallium-implanted poly Si layers and compared it with in situ boron-doped, plasma-enhanced chemical vapor deposition (PECVD) poly Si layers. Although they reported very high $iV_{OC} = 735$ mV for gallium-doped poly Si/SiO₂ layers, their boron-doped poly Si/SiO₂ stacks showed only a mild passivation quality with $iV_{OC} = 700$ mV.

In the present work, we show that achieving high passivation quality is possible even with boron as a dopant species for hole-selective poly Si/SiO₂ layers without the need for ion implantation, which is considered a costly process step in the PV industry. We use a green laser for boron activation on low-pressure chemical vapor deposition (LPCVD) poly Si layers that results in high passivation quality with $iV_{OC} = 720$ mV. Additionally, we consider here the role of interfacial SiO₂ in the laser crystallization of poly Si layers.

2. Sample Preparation

In this work, we design two types of test structures to study the effect of laser processing parameters on the electrical characteristics and the passivation quality of the poly Si/SiO₂ double layers. To investigate the influence of the interfacial oxide and poly Si layer thickness on these test structures, we use two poly Si layer thicknesses in our samples and also prepare groups of samples without interfacial oxide.

Our process starts with commercially available as-cut n-type M2 size Czochralski (Cz) silicon substrates from LONGi with a base resistivity of 27 Ω cm. After saw-damage etching and cleaning in a mixture of sulfuric acid (H₂SO₄) and hydrogen peroxide (H₂O₂),

the wafers are split into two groups. One group is thermally oxidized in a tube process to create the SiO_2 with a thickness of about 2 nm, while the other group is further processed without SiO_2 . Accordingly, an intrinsic hydrogen-free amorphous silicon (a-Si) thin film is deposited via LPCVD. Next, the intrinsic a-Si films are lightly doped in our BBr_3 diffusion furnace at diffusion temperature $T_{\text{diff}} = 820$ °C. The a-Si layers are partially crystallized during this high temperature step. We extract the grain size $d_g \approx 6$ nm after the BBr_3 diffusion step from the peak analysis of X-ray diffraction (XRD) measurement. Thereafter, borosilicate glass (BSG) created during the diffusion is removed in 2% hydrofluoric acid (HF). The subsequent laser process is performed on square-shaped fields with an area $A_{\text{laser-field}} = 38 \times 38 \text{ mm}^2$, using a nanosecond laser tool operating at a wavelength $\lambda = 532$ nm, with a rectangular-shaped tophat laser beam profile and a spot area $A_{\text{spot}} = 300 \times 600 \mu\text{m}^2$. The XRD measurements show the grain size growth from $d_g \approx 6$ nm for non-lasered layers to $d_g \approx 20$ nm for laser-crystallized poly Si layers (L-poly Si). Two poly Si thicknesses are examined for both groups of samples, with and without a SiO_2 layer.

The thickness of the poly Si films is measured with spectral ellipsometry on dedicated test wafers. The thicknesses are determined as $d_{\text{poly Si},1} = 155 \text{ nm} \pm 5 \text{ nm}$ and $d_{\text{poly Si},2} = 264 \text{ nm} \pm 9 \text{ nm}$.

The amount of energy carried by each laser pulse is a crucial parameter for adjusting the later doping profile and, consequently, the electrical properties of the doped layers. The area normalized energy per pulse is called the laser pulse energy density (H_p). A detailed definition of H_p is given in ref. [20]. The H_p is varied by changing the laser duty cycle at the same pulse repetition rate $f = 10$ kHz with a pulse duration $\tau_p \approx 100$ ns. A laser pulse overlap of 10% is used in both the y-direction (scanning direction) and the x-direction to ensure full area coverage and short laser processing time. Two kinds of test structures are fabricated:

- Sheet resistance R_{sh} samples to characterize the electrical properties of the laser-processed samples, e.g., by four-point-probe measurement of the sheet resistance and by electrochemical capacitance/voltage (ECV) measurements of the doping profile.
- Symmetric passivation samples for assessing the passivation quality with quasi-steady-state photoconductance QSSPC measurements [21].

Figure 2a shows a schematic cross-section of a fabricated R_{sh} sample, while a cross-section of a passivation sample is shown in Figure 2b. Although test structures without SiO_2 are also fabricated, only samples with SiO_2 are shown in Figure 2a,b for the sake of simplicity.

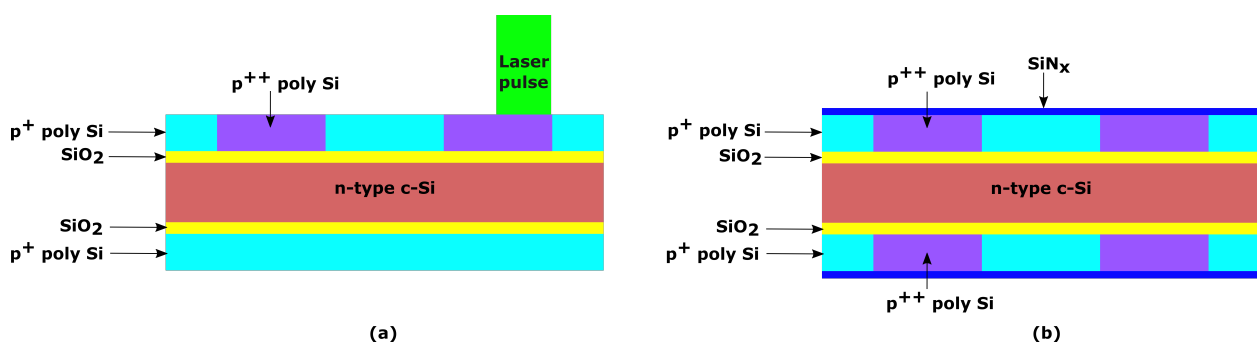


Figure 2. (a) Schematic cross-section of the R_{sh} samples. Laser irradiation increases the doping concentration by activating boron atoms in the p^+ poly Si layer. The electrical properties of the irradiated regions are characterized by R_{sh} and ECV measurements. (b) Symmetric passivation samples for QSSPC measurements. The front and rear sides of the samples are irradiated symmetrically, which is followed by an extra high temperature annealing step and $\text{SiN}_x\text{:H}$ deposition on both the front and rear sides. Note that test structures without SiO_2 are also fabricated. However, for the sake of simplicity, only samples containing SiO_2 are shown.

In order to imitate a complete solar cell fabrication process with diffusion and annealing steps, an additional annealing step at temperature $T_{\text{anneal}} = 985 \text{ }^\circ\text{C}$ for a time $t_{\text{anneal}} = 30 \text{ min}$ at ambient nitrogen is also applied to the passivation samples. Later, using PECVD, a silicon nitride ($\text{SiN}_x\text{:H}$) layer (which serves as a hydrogen source for passivation) is deposited on both sides of the lifetime samples. At this stage, the passivation quality of the samples is measured by QSSPC and photoluminescence (PL) measurements.

3. Laser Activation

3.1. Sheet Conductance

Figure 3a,b show the measured sheet conductances (G_{sh}) for different H_p c-Si/SiO₂/poly Si and c-Si/poly Si structures. The G_{sh} -values are obtained by converting the measured R_{sh} -values to

$$G_{sh} = 1/R_{sh}. \quad (1)$$

The G_{sh} -values of the samples with both the tested poly Si layer thicknesses can be divided into four zones based on the different dependence on H_p :

- **Zone I, background doping:** All measured G_{sh} values are in the range of the background doping, which is created during the BBr_3 diffusion. The background doping is measured from non-lasered areas on the wafer ($H_p = 0 \text{ J/cm}^2$). Hence, no laser activation of dopants is observed in this zone.
- **Zone II, activation:** For both groups of samples, with and without interfacial oxide, G_{sh} starts to increase when the laser pulse begins to melt the poly Si layer at the poly Si melting threshold $H_p \approx 1 \text{ J/cm}^2$. For $H_p \geq 1 \text{ J/cm}^2$, G_{sh} linearly increases with increasing H_p , which shows an increased number of electrically active boron atoms.
- **Zone III, saturation:** The G_{sh} -values of the samples without SiO₂ start to differ from the G_{sh} -values of samples with SiO₂. The measured difference will be discussed in more detail in Section 5. However, both groups have in common that increasing H_p further does not significantly increase the G_{sh} .
- **Zone IV, SiO₂-destruction:** A sudden increase in G_{sh} of samples with SiO₂ is observed in this zone, rendering it identical to the value measured for the samples without SiO₂.

Figure 3a compares the measured G_{sh} of the samples with and without SiO₂ for the structures with the poly Si layer thickness $d_{\text{poly Si},1} = 155 \text{ nm}$. In zones I and II ($H_p \leq 2 \text{ J/cm}^2$), the same G_{sh} -values are measured for both sample types with and without SiO₂, indicating that the presence or absence of the SiO₂ does not affect the activation process. The G_{sh} starts to increase linearly from the melting threshold laser pulse energy density $H_p \approx 1 \text{ J/cm}^2$ until $H_p = 2 \text{ J/cm}^2$. The H_p at the transition from zone II to zone III is called the transition laser pulse energy density (H_T) in the following. The SiO₂ affects the measured G_{sh} in zone III, where laser pulse energy densities above the H_T are used. The G_{sh} of samples with SiO₂ saturates around the average sheet conductance $G_{sh-ave.} = 19.6 \pm 3.3 \text{ mS sq}$, while higher $G_{sh-ave.} = 65.6 \pm 7.3 \text{ mS sq}$ is measured for samples without SiO₂. In zone IV, the highest $H_p = 5 \text{ J/cm}^2$ results in similar G_{sh} -values for samples with and without SiO₂.

Figure 3b compares the measured G_{sh} of samples with a thicker poly Si layer with the thickness $d_{\text{poly Si},2} = 264 \text{ nm}$ in the presence and absence of SiO₂. Similar to the samples with a thinner poly Si layer, in zones I and II, presence of SiO₂ does not significantly influence the measured G_{sh} -values. The activation threshold H_p remains unchanged at $H_p \approx 1 \text{ J/cm}^2$, as was observed for samples with a poly Si layer of $d_{\text{poly Si},1} = 155 \text{ nm}$. However, the H_T from zone II to zone III is shifted from $H_p = 2 \text{ J/cm}^2$ to $H_p = 2.8 \text{ J/cm}^2$ for the samples with a thicker poly Si layer. In zone IV, the same G_{sh} -values for both structures are measured. Similar behavior is also observed for samples with thinner poly Si layers.

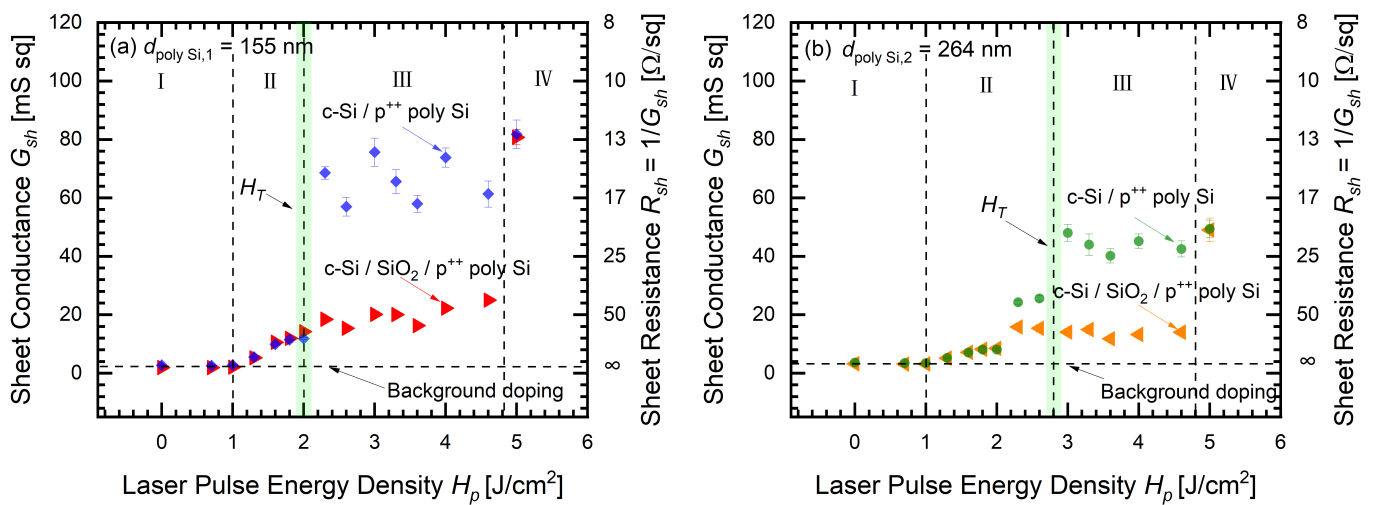


Figure 3. Sheet conductances G_{sh} and measured sheet resistances R_{sh} of samples with and without SiO₂ for poly Si thicknesses $d_{poly Si,1} = 155$ nm and $d_{poly Si,2} = 264$ nm. (a) For both types of samples, the activation process starts at $H_p \approx 1$ J/cm², where G_{sh} begins to increase linearly with increasing H_p . The presence of SiO₂ starts to influence the G_{sh} when H_p exceeds the transition energy $H_T = 2$ J/cm². For 2.3 J/cm² $\leq H_p \leq 4.6$ J/cm², the G_{sh} of samples without SiO₂ saturates at higher values compared to samples including the SiO₂. The $H_p = 5$ J/cm² significantly increases the G_{sh} of samples with SiO₂, and results in the same G_{sh} for samples with and without SiO₂. (b) For $d_{poly Si,2} = 264$ nm samples, the activation H_p remains unchanged. However, the H_T increases to $H_p = 2.8$ J/cm². Similar to the samples with a thinner poly Si layer, $H_p = 5$ J/cm² results in the same G_{sh} -values for samples with and without SiO₂.

3.2. Progressive Melting of Poly Si

Figure 4a shows the ECV profiles of poly Si/SiO₂/c-Si samples processed with low to intermediate H_p for poly Si layers with thickness $d_{poly Si,1} = 155$ nm. The $H_p = 0$ J/cm² represents the background doping taken from the samples without laser processing. The lowest used laser pulse energy density $H_p = 0.7$ J/cm² does not change the background doping. Melting of the poly Si layer starts when H_p reaches the melting threshold $H_p = 1$ J/cm², where the concentration at the surface is marginally increased. This is compatible with the melting threshold found in Figure 3a,b. For $H_p \geq 1$ J/cm², higher concentrations are measured with respect to the background doping, and the depth of the part of the profiles with high doping concentrations progressively increases with increasing H_p . This behavior indicates the progressive melting of the poly Si layer. After absorbing a laser pulse with sufficient energy to melt the poly-Si, the poly Si layer begins to melt from the surface, and the melt front propagates into the depth of the poly Si layer. Increasing the H_p , increases the Si melt propagation, resulting in deeper ECV profiles with high concentrations.

Figure 4b shows the doping profiles of samples including SiO₂ processed with high H_p . The flat profiles with constant doping concentrations across the whole poly Si layer thickness for 2.3 J/cm² $\leq H_p \leq 4$ J/cm² show that the laser pulse fully melts the poly Si layer. The sharp drop in the concentrations approximately at the position of the SiO₂ indicates that even this very thin passivating SiO₂ stops the Si melt propagation. A deeper profile inside the c-Si substrate for $H_p = 4.6$ J/cm² compared to the lower laser pulse energy densities implies that the effectiveness of the SiO₂ as a diffusion barrier starts to degrade at this H_p . This shows that the SiO₂ is increasingly damaged for $H_p > 4$ J/cm², which eventually results in destroyed SiO₂ for $H_p = 5$ J/cm², represented by a reduced boron concentration within the first 150 nm of the profile and the deepest profile inside the substrate. The effect of damaged and destroyed SiO₂ on passivation will be shown in Section 6.

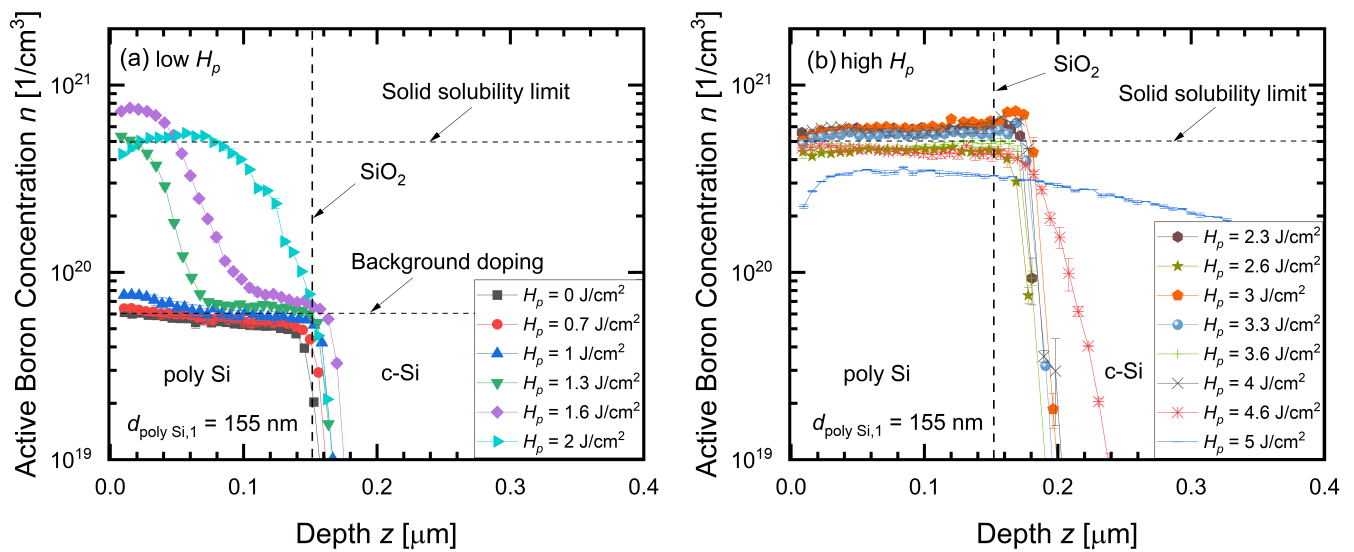


Figure 4. (a) ECV profiles of the laser-processed samples for $H_p \leq 2 \text{ J/cm}^2$ with a poly Si layer thickness $d_{\text{poly Si},1} = 155 \text{ nm}$. Laser activation starts at a melting threshold laser pulse energy density $H_p = 1 \text{ J/cm}^2$ where a slightly higher surface concentration than the background doping is measured. For H_p beyond the melting threshold ($H_p \geq 1.3 \text{ J/cm}^2$), increasing H_p increases the Si melt propagation, resulting in deeper ECV profiles with high concentrations. The depth of the ECV profiles with high concentration progressively increases by increasing the H_p . (b) High laser pulse energy densities $H_p \geq 2.3 \text{ J/cm}^2$ melt the entire $d_{\text{poly Si},1} = 155 \text{ nm}$ thick layer and create flat ECV profiles. The SiO_2 prevents the Si melt transfer to the c-Si bulk up to $H_p = 4 \text{ J/cm}^2$, creating a sharp drop in high concentrations at the position of the SiO_2 . Higher $H_p = 4.6 \text{ J/cm}^2$ damages the SiO_2 and results in a deeper doping tail compared to lower H_p . Finally, $H_p = 5 \text{ J/cm}^2$ destroys the SiO_2 and pushes boron atoms into the c-Si substrate, resulting in a reduced boron concentration within the first 150 nm of the profile.

3.2.1. Supersaturation

Figure 4a also shows the peak concentrations. For $H_p \geq 1.3 \text{ J/cm}^2$, they exceed the solid solubility limit of boron in Si, which amounts to $s_{\text{max}} \approx 5 \times 10^{20} \text{ cm}^{-3}$ at $1200 \text{ }^\circ\text{C}$ [10]. This finding indicates that the laser-activated poly Si layers are supersaturated with boron atoms. Grain boundaries in poly Si provide an easy path for boron atoms to diffuse, and, therefore, allow for high dopant diffusivity [22]. We speculate that rapid boron migration along this path strongly enhances boron diffusion during the furnace BBr_3 diffusion step in our experiment. However, not all boron atoms from BBr_3 diffusion are electrically active. For example, boron atoms located at grain boundaries are not electrically active and, therefore, are not detectable with ECV measurements. The background doping shown in Figure 4a represents only the electrically active boron concentration from the BBr_3 diffusion step. After melting the poly Si layer with a laser pulse, boron atoms diffuse into the molten Si due to a significantly higher diffusion coefficient D of boron in molten Si ($D_l \approx 10^{-4} \text{ cm}^2/\text{s}$ in liquid [23]) compared to the solid Si ($D_s \approx 10^{-11} \text{ cm}^2/\text{s}$ in solid at $1150 \text{ }^\circ\text{C}$ [24]). Directly after the laser pulse, the molten Si recrystallizes rapidly, and dopant impurities are frozen into the Si lattice where they are electrically active. This results in an increase in electrically active boron concentrations beyond the conventional solid solubility limit [? ?].

A high active boron concentration of p^{++} -poly Si has several advantages for the processing of solar cells:

- (i) It is essential for obtaining a low contact resistance at the metal/semiconductor contact interface [9]. It was shown earlier that just the conventional maximum solid solubility of boron in silicon is a limiting factor in contacting boron-doped p^+ -poly Si layers, which are fabricated with a conventional furnace-based process [11].

- (ii) A high active boron concentration provides an etch stop in potassium hydroxide (KOH) solution and, therefore, enables the maskless patterning of p^{++} poly layers, as described in ref. [15].

Unfortunately, however, supersaturation is not a stable condition, and a high temperature post-annealing step usually results in a reduction in the electrically active dopant concentrations to an equilibrium level [28, 29]. We also detect a reduction in the active boron concentration in our lifetime samples, which undergo an additional high temperature step. However, if the selective etching is carried out before the high temperature step, the maskless patterning of the p^{++} -poly Si layer is still possible. At present, we are investigating this effect in a separate study, which will be reported in a future publication.

3.2.2. Melt Depth Extraction

Figure 5a shows the progressive melting of a $d_{\text{poly Si},2} = 264$ -nm-thick layer in poly Si/SiO₂/c-Si samples. Similar to the thinner poly Si layers in Figure 4a, increasing H_p results in deeper ECV profiles with high concentrations. We use this behavior to determine the approximate melt depth (d_{melt}) created by different laser pulse energy densities H_p . Assuming that the melting of the poly Si layer increases the doping concentration, those parts of the ECV profiles with higher concentrations than the background doping are considered the molten parts of the poly Si layer. Accordingly, the transition depth, where the measured ECV profiles drop back to the non-melted level, is extracted as the approximate d_{melt} . A possible diffusion of dopants within the solid part of the layer is neglected here. The determined d_{melt} for each H_p is indicated by a vertical dashed line in Figure 5a.

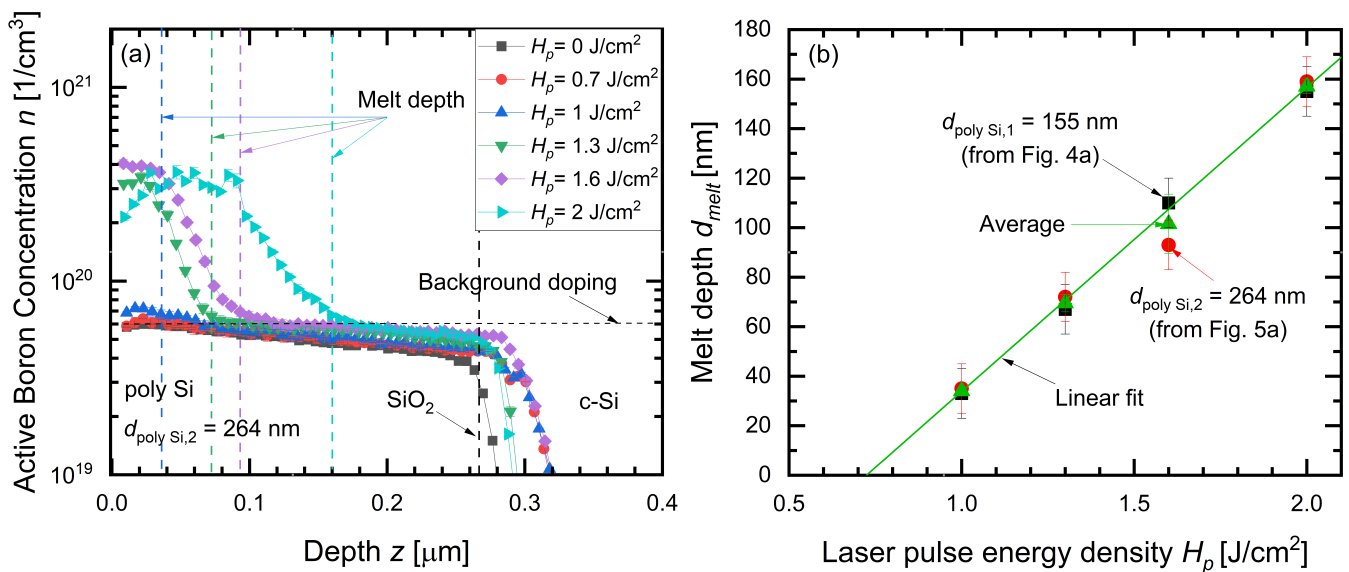


Figure 5. (a) Doping profiles used for the d_{melt} determination of samples with a poly Si layer thickness of $d_{\text{poly Si},2} = 264$ nm. The melt depth (indicated by dashed lines) of each H_p is selected as a depth where the high concentration at the surface drops back to the non-melted background doping level. (b) The extracted and average d_{melt} for $d_{\text{poly Si},1} = 155$ nm and $d_{\text{poly Si},2} = 264$ nm poly Si layers in zone II ($1 \text{ J/cm}^2 \leq H_p \leq 2 \text{ J/cm}^2$). For both poly Si layers, the d_{melt} increases linearly with increasing H_p .

Figure 5b illustrates the extracted melt depth for poly Si layers with $d_{\text{poly Si},1} = 155$ nm (from Figure 4a) and $d_{\text{poly Si},2} = 264$ nm (from Figure 5b). For both poly Si layers, the d_{melt} linearly increases with increasing H_p . This behavior for poly Si agrees with the earlier observed linear dependence of d_{melt} on the H_p in the laser processing of conventional bulk c-Si [20,30]. However, the melting rate found in ref. [20] for c-Si is about four times higher than the melting rate found here for poly Si. This is explained by us by the different thermal conductivities of poly Si and bulk c-Si structures. The thermal conductivity $k_{\text{poly Si}}$ of a boron-doped poly Si layer at $T = 300$ K with a grain size $d_g \approx 400$ nm and a doping

concentration $n = 1.6 \times 10^{19} \text{ cm}^{-3}$ was extracted as $k_{\text{poly Si}} = 45.6 \text{ W/mK}$ in [31], while the thermal conductivity of undoped c-Si at the same temperature is $k_{\text{c-Si}} = 148 \text{ W/mK}$ [32].

In the case of our poly Si, a similar d_{melt} is extracted for both layers for each H_p . This behavior is expected since the melting of the poly Si layer starts from the surface. The similar extracted melt depth allows us to apply a linear fit to the average d_{melt} and to calculate the melting rate. The linear fit in Figure 5b shows that melting of poly Si starts at $H_p = 0.7 \text{ J/cm}^2$ and increases linearly with a rate of $122 \text{ nm/(J/cm}^2)$. This extrapolation predicts that the melt front reaches the poly Si/SiO₂ interface at $H_p = 1.9 \text{ J/cm}^2$ and $H_p = 2.8 \text{ J/cm}^2$ for $d_{\text{poly Si},1} = 155 \text{ nm}$ and $d_{\text{poly Si},2} = 264 \text{ nm}$ structures, respectively. These values agree with the G_{sh} data shown in Figure 3a,b. The same laser pulse energy densities are found there as the H_T from zone II to zone III.

Figure 6 shows the dependency of G_{sh} on the melt depth in zone II. The G_{sh} increases linearly for both poly Si layers, indicating that the number of electrically active boron atoms also increases linearly with increasing d_{melt} . However, the slope of the linear fit for the $d_{\text{poly Si},1} = 155 \text{ nm}$ samples is higher compared to $d_{\text{poly Si},2} = 264 \text{ nm}$. This difference is attributed to the total number of distributed boron atoms in these poly Si layers. We assume that the total number of boron atoms stored in these two poly Si layers is equal because of the same BBr₃ diffusion step. Hence, the boron atoms are distributed more densely in the $d_{\text{poly Si},1} = 155 \text{ nm}$ poly Si layer compared to the $d_{\text{poly Si},2} = 264 \text{ nm}$ poly Si layer. Thus, the same melt depth results in a higher number of activated boron atoms for the $d_{\text{poly Si},1} = 155 \text{ nm}$ poly Si layer compared to the layer with the thickness $d_{\text{poly Si},2} = 264 \text{ nm}$. The reason for the higher G_{sh} of $d_{\text{poly Si},2} = 264 \text{ nm}$ samples at the beginning of the melting zone in Figure 6 is not clear and requires more investigation.

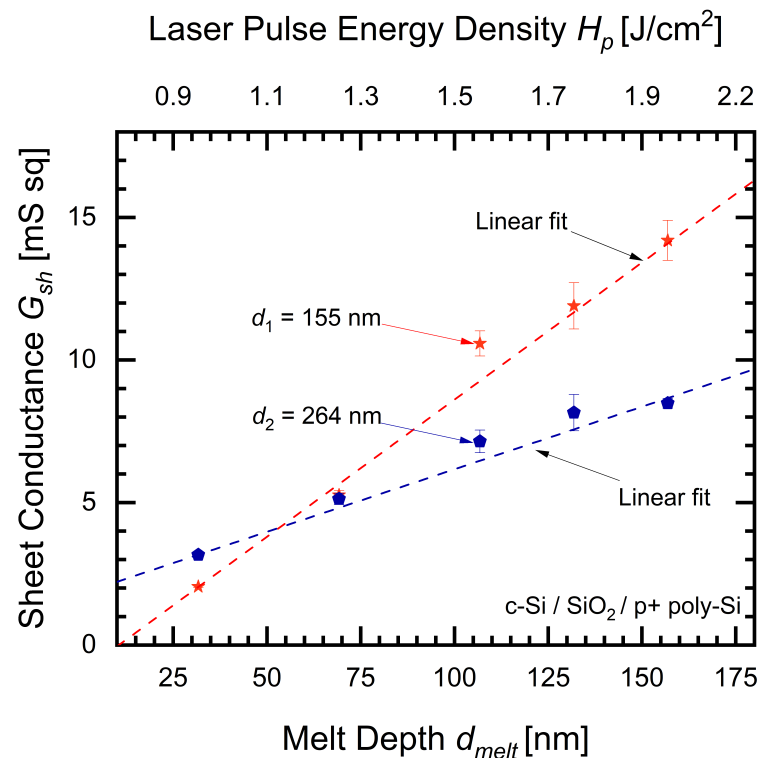


Figure 6. The measured G_{sh} of the c-Si/SiO₂/p⁺-poly Si samples in zone II. The G_{sh} of both poly Si layers linearly increases with increase in the d_{melt} , suggesting that the quantity of incorporated boron atoms in conduction also increases by increasing d_{melt} . Due to the equal total number of boron atoms from the same BBr₃ diffusion step, boron atoms are distributed more densely in the $d_{\text{poly Si},1} = 155 \text{ nm}$ samples, resulting in a higher number of active boron atoms in the $d_{\text{poly Si},1} = 155 \text{ nm}$ samples compared to $d_{\text{poly Si},2} = 264 \text{ nm}$ for the same melt depth.

3.3. Role of Interfacial Oxide in Electrical Properties

Figure 7 shows the doping profiles for the four different laser activation zones for samples with and without SiO_2 . In zone I ($H_p = 0 \text{ J/cm}^2$), no laser processing is performed, and, hence, the active boron concentration after the initial (furnace) boron diffusion is shown. The measured value agrees with the solubility limit of boron in Si at the BBr_3 diffusion temperature $T_{\text{diff}} = 820 \text{ }^\circ\text{C}$ [24]. The presence of the SiO_2 creates only a minor difference between the ECV profiles of samples with and without SiO_2 in this zone. Diffusion of boron into c-Si is more pronounced for samples without SiO_2 . In zone II, where the used H_p exceeds the threshold H_p of poly Si melting, the active boron concentrations above the background doping are measured at the surface of poly Si. However, the concentration decreases from the surface to the depth of the poly Si layer, implying a partial melting of the poly Si layers. The poly Si layer is only partially melted by $H_p = 1.3 \text{ J/cm}^2$, and the melt front is stopped before reaching the poly Si/ SiO_2 or the poly Si/c-Si interface. Thus, the presence or absence of SiO_2 does not influence the doping of the poly Si layers in this zone. In zone III, for both sample types with and without SiO_2 , $H_p = 3 \text{ J/cm}^2$ results in a consistent and high doping concentration in the depth of the entire poly Si layer, which indicates melting of the entire poly Si layer. For samples with SiO_2 , the boron concentration is strongly reduced at the approximate position of the SiO_2 , showing that SiO_2 blocks the Si melt front from propagating into the bulk c-Si wafer. A deep profile in the c-Si substrate is measured for samples without SiO_2 , which leads to higher measured G_{shr} , as shown in Figure 3a,b. In zone IV, similar ECV profiles for samples with and without SiO_2 indicate that the Si melt front created by $H_p = 5 \text{ J/cm}^2$ destroys the SiO_2 and propagates into the c-Si bulk wafer.

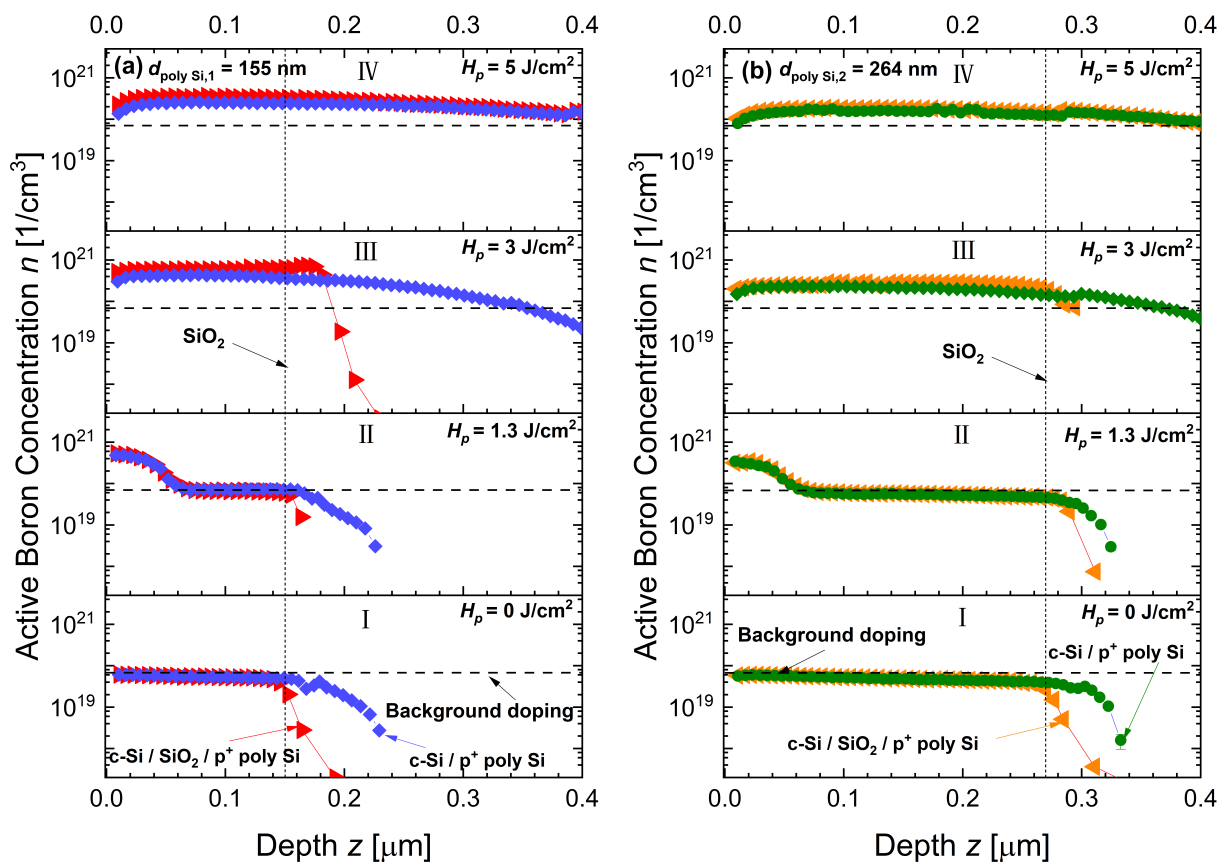


Figure 7. ECV profiles of samples with and without SiO_2 (position of SiO_2 is marked) with the poly Si layer thicknesses $d_{\text{poly Si},1} = 155 \text{ nm}$ and $d_{\text{poly Si},2} = 264 \text{ nm}$. In zone I ($H_p = 0 \text{ J/cm}^2$), for both poly

Si layers in (a,b), similar doping profiles are measured for structures with and without SiO₂. These profiles represent the background doping after the BBr₃ furnace diffusion. The presence of SiO₂ plays a minor role in the background doping by limiting the boron diffusion in c-Si for samples with SiO₂ in this zone. In zone II, $H_p = 1.3 \text{ J/cm}^2$ results in ECV profiles with high active boron concentrations at the surface of the poly Si layers, which decrease towards the depth and reach the background doping level. Thus, the SiO₂ does not significantly influence the electrical properties of $d_{\text{poly Si},1} = 155 \text{ nm}$ and $d_{\text{poly Si},2} = 264 \text{ nm}$ samples. In Zone III, for samples with both poly Si layers, samples with SiO₂ show a significant reduction in boron concentration at the position of SiO₂, while for samples without SiO₂, a deep profile inside c-Si is measured. In zone IV, $H_p = 5 \text{ J/cm}^2$ creates similar ECV profiles for samples with and without SiO₂ for both poly Si layers, which suggests the destruction of SiO₂.

4. Charge Carrier Mobility in Laser-Activated Poly Si

Due to the presence of grain boundaries, the charge carrier mobility in poly Si is expected to be lower than that for monocrystalline silicon for the same doping concentrations [?]. The average mobility μ in our doped semiconductor layers with a diffusion profile is calculated by us from

$$\mu = \frac{G_{sh}}{q \int_0^x n(x) dx} , \quad (2a)$$

where G_{sh} is the sheet conductance, q is the elementary charge, and $n(x)$ is the depth-depending doping concentration. With the depth integrated average doping dose or sheet concentration $\bar{N}_{sh} = \int_0^x n(x) dx$, Equation (2a) becomes

$$\mu = \frac{G_{sh}}{q \bar{N}_{sh}} . \quad (2b)$$

We calculate the hole mobility in laser-activated poly Si layers with Equation (2b), using the G_{sh} -values from four-point-probe measurements and by integrating the ECV profiles over the depth, which provides \bar{N}_{sh} . Due to the different doping types of the substrate and laser-processed poly Si layers, the substrate does not contribute to the R_{sh} measurements for the sample structures used here (see Figure 2a).

Figure 8 shows the \bar{N}_{sh} versus the H_p for structures with SiO₂. For both poly Si thicknesses, \bar{N}_{sh} increases for $H_p \geq 1 \text{ J/cm}^2$ and saturates in zone III, which is similar to the behavior of G_{sh} in Figure 3a,b. Based on the constant values of \bar{N}_{sh} in the regime $2.3 \text{ J/cm}^2 \leq H_p \leq 4.6 \text{ J/cm}^2$, we use the average \bar{N}_{sh} value for the hole mobility calculation. The mentioned H_p range also results in a similar G_{sh} -values, as is shown in Figure 3a,b, which makes it possible to use the average G_{sh} -values for hole mobility calculation.

Table 1 shows the utilized data for the hole mobility calculation in poly Si and compares the calculated hole mobility in poly Si with the hole mobility in c-Si for a similar average boron concentration around $\bar{n} = 4 \times 10^{20} \text{ cm}^{-3}$. The average boron concentration \bar{n} in poly Si layers is estimated by dividing \bar{N}_{sh} by the respective thickness of the poly Si layers through

$$\bar{n} = \frac{\bar{N}_{sh}}{d_{\text{poly Si}}} . \quad (3)$$

The calculated hole mobility values are comparable for both poly Si layer thicknesses. Hence, we consider the average value of $\mu_{\text{poly Si}} \approx 15 \text{ cm}^2\text{V}^{-1}\text{s}^{-1}$ as the hole mobility in this work, which compares well to that calculated in ref. [34] as $\mu \approx 14 \text{ cm}^2\text{V}^{-1}\text{s}^{-1}$ for boron-doped poly Si layers.

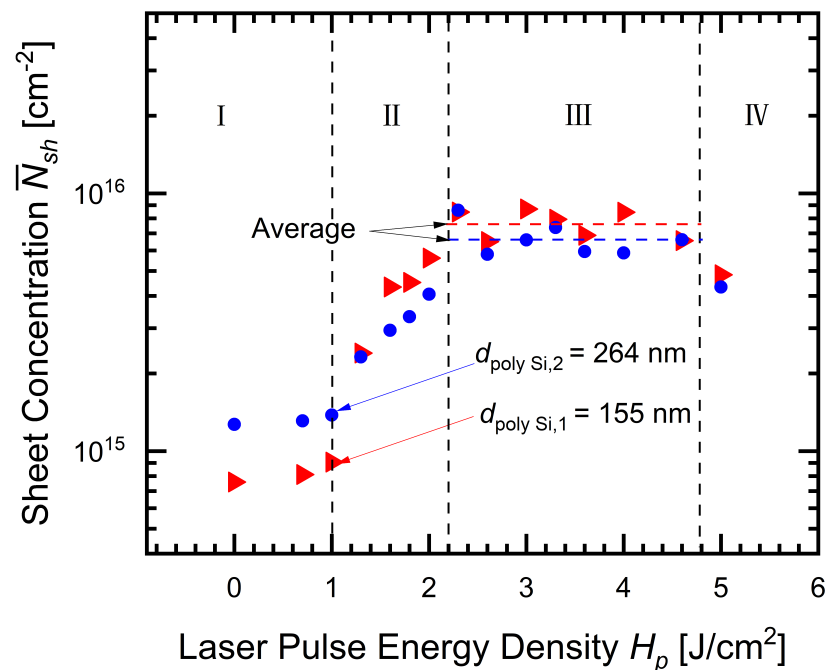


Figure 8. Extracted \bar{N}_{sh} for samples with SiO₂ and poly Si layer thicknesses of $d_{poly\ Si,1} = 155$ nm and $d_{poly\ Si,2} = 264$ nm. For both poly Si layers, \bar{N}_{sh} saturates in zone III. The average \bar{N}_{sh} values in this zone are used for the hole mobility derivation.

Table 1. Input data for hole mobility μ calculation and calculated hole mobility in poly Si for two different thicknesses.

Structure	\bar{n} [cm ⁻³]	\bar{N}_{sh} [cm ⁻²]	G_{sh} [mS sq]	μ [cm ² V ⁻¹ s ⁻¹]
155 nm poly Si	$(4.8 \pm 0.9) \times 10^{20}$	$(7.6 \pm 1) \times 10^{15}$	19.6 ± 3.3	16.0 ± 2.6
264 nm poly Si	$(2.4 \pm 0.4) \times 10^{20}$	$(6.6 \pm 1) \times 10^{15}$	14.1 ± 1.3	13.1 ± 1.2
c-Si	4×10^{20}	-	-	40 [35]

5. Role of SiO₂ in Poly Si Crystallization in the Saturation Zone

Figure 3a,b, in zone III, show significantly higher measured G_{sh} -values for samples without SiO₂ compared to G_{sh} -values of samples with SiO₂. In this section, we formulate two hypotheses to explain the measured difference in the G_{sh} -values of samples with and without SiO₂. Accordingly, we calculate the expected G_{sh} from ECV profiles for each hypothesis and compare them with the measured G_{sh} -values. We perform the analysis for samples with a poly Si layer thickness $d_{poly\ Si,1} = 155$ nm.

5.1. Hypothesis A

The higher G_{sh} -value in zone III for samples without SiO₂ (see $H_p = 3$ J/cm² in Figure 7a) stems from the extent of the doping tail into the bulk material. Therefore, the doping tail in the bulk leads to higher measured G_{sh} . For the test of this hypothesis A, we assume that the ECV profile is composed of two parts, (i) a highly doped laser-crystallized poly Si L-poly Si with a thickness $d_{poly\ Si,1} = 155$ nm, and (ii) a sheet of highly doped mono-crystalline Si. Because of a different charge carrier mobility in L-poly Si and c-Si, the contribution of each structure in the total G_{sh} is calculated individually.

5.2. Hypothesis B

We ascribe the higher sheet conductance for samples without oxide to a seeded crystallization of the poly Si to become single crystalline Si with a higher mobility: In the absence of SiO₂ for $H_p > H_T$ in zone III, the Si melt reaches the poly Si/c-Si interface and melts a portion of the c-Si substrate. In the crystallization process, the single-crystalline bulk silicon acts as a seed layer. Then, via liquid phase epitaxy, the molten poly Si regrows as a single crystalline layer. Due to the lack of grain boundaries in the solidified single crystal Si, the charge carrier mobility of the solidified Si layer approaches the carrier mobility of single crystalline Si and results in high G_{sh} -values.

5.2.1. G_{sh} -Data from Hypothesis A

Figure 9a visualizes the G_{sh} -calculation from the ECV profiles using hypothesis A. For estimating the contribution of the highly doped L-poly Si layer to the total G_{sh} , we use the derived hole mobility value in Section 4 ($\mu_{poly\ Si} = 15\ \text{cm}^2\text{V}^{-1}\text{s}^{-1}$) within the thickness $d_{poly\ Si,1} = 155\ \text{nm}$ of the poly Si layer. For calculating the share of a highly doped mono-crystalline Si sheet from the part of the ECV profiles beyond 155 nm, we use the PV lighthouse R_{sh} calculator tool, which calculates the corresponding R_{sh} of an ECV profile for a c-Si structure [36].

5.2.2. G_{sh} -Data from Hypothesis B

Figure 9b depicts the G_{sh} calculation utilizing hypothesis B. In hypothesis B, we assume the poly Si/c-Si structure recrystallizes to a c-Si/c-Si structure when the H_p is higher than the H_T . Hence, to calculate the G_{sh} -values using hypothesis B, we consider the same hole mobility of c-Si for a recrystallized c-Si/c-Si structure, which enables us to also use the R_{sh} calculator tool of PV lighthouse.

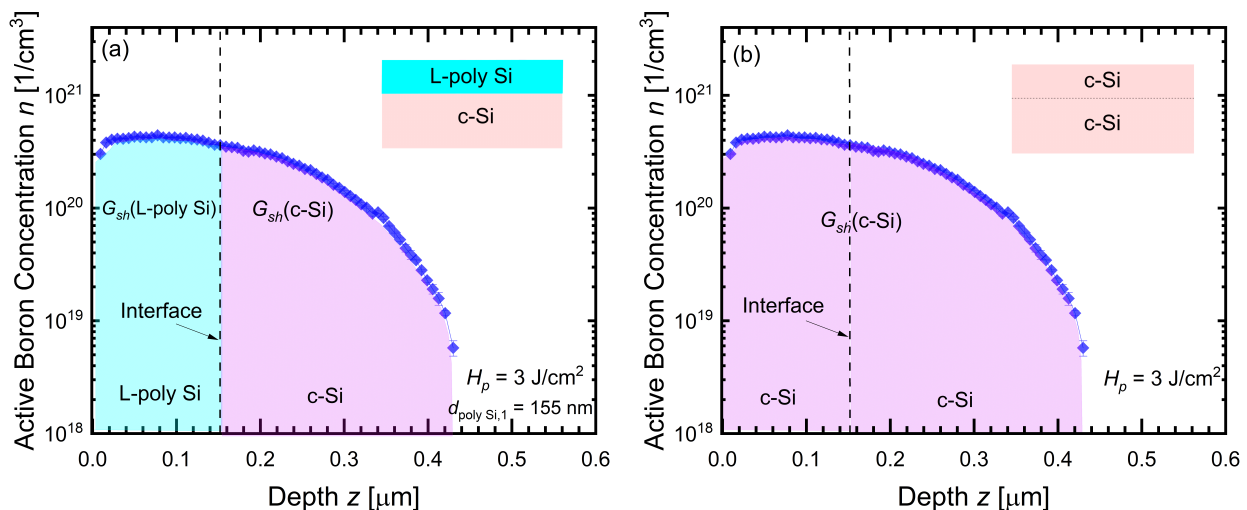


Figure 9. Employed hypotheses in the G_{sh} calculation from the ECV profiles for samples without SiO₂. (a) Hypothesis A considers the recrystallized structures as the combination of L-poly Si and c-Si. The G_{sh} in the L-poly Si part, indicated in cyan, is calculated for the first 155 nm of the doping profile from the surface using the determined hole mobility of $\mu_{poly\ Si} \approx 15\ \text{cm}^2\text{V}^{-1}\text{s}^{-1}$. The contribution of the doped c-Si part, highlighted in magenta, is determined with the PV lighthouse R_{sh} calculator tool. (b) Hypothesis B assumes that, for $H_p \geq 2.3\ \text{J}/\text{cm}^2$, the Si melt extends to the c-Si substrate seed layer and recrystallizes to a mono-crystal Si layer via liquid phase epitaxy. This results in a c-Si/c-Si structure with the same hole mobility as c-Si. The final G_{sh} (c-Si) is also determined via the PV lighthouse R_{sh} calculator tool.

5.2.3. Comparison of Hypotheses for Samples without SiO₂

The comparison in Figure 10 shows that hypothesis B explains the measured data better. The figure compares the expected G_{sh} values considering hypothesis A with the measured G_{sh} data shown in Figure 3a. For H_p less than the H_T ($H_p < 2.3 \text{ J/cm}^2$), where the Si melt does not propagate into the c-Si substrate, hypothesis A is in close agreement with the measured G_{sh} data. However, for $H_p \geq 2.3 \text{ J/cm}^2$, where the Si melt extends to the underlying c-Si substrate, hypothesis A predicts lower G_{sh} -values than the measured data, indicating that the high G_{sh} -values in zone III for samples without SiO₂ cannot solely be explained by the deeper doping profile. For $H_p \geq 2.3 \text{ J/cm}^2$, the prediction by hypothesis B is in better agreement with the measured data than the prediction by hypothesis A. From this comparison, we conclude that the recrystallized structure is a c-Si/c-Si structure, as assumed by hypothesis B. Similar re-crystallization of the pre-amorphized poly Si layers to a single-crystal structure via liquid phase epitaxy during the laser annealing is also described elsewhere [28?].

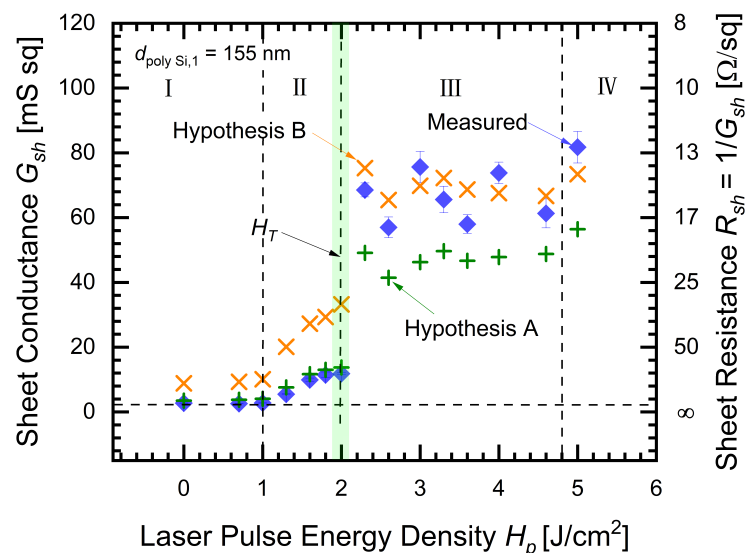


Figure 10. Comparison of measured G_{sh} from layers without SiO₂ with expected G_{sh} when considering the mobility of L-poly Si within the first 155 nm of the sample (hypothesis A) and when considering the mobility of c-Si for the entire samples structure (hypothesis B). For H_p less than the H_T , in which the Si melt is not extended to the c-Si substrate, the measured G_{sh} -values agree with the predicted G_{sh} -values of hypothesis A, suggesting that the Si melt recrystallizes to an L-poly Si structure. However, when H_p exceeds the H_T , the predicted G_{sh} -values by hypothesis B agree with the measured G_{sh} -values indicating that the Si melt recrystallizes to a mono-crystal layer with comparable carrier mobility to a single-crystal structure.

5.2.4. Comparison of Hypotheses for Samples with SiO₂

To examine the influence of SiO₂ in the crystallization process, we apply the same methodology as described above for samples with SiO₂. Figure 11 shows a comparison of the measured G_{sh} -values and the values predicted by hypotheses A and B. In zones I, and II, estimated values by hypothesis A show better agreement with the measured values, as also found above. However, here, hypothesis A also fits better in zone III, in contrast to the result for structures without SiO₂. This difference shows that the SiO₂ prevents the Si melt propagation to the c-Si substrate. Hence, no lattice information from the substrate is available, and the Si melt recrystallizes to an L-poly Si structure.

In zone IV, for the highest $H_p = 5 \text{ J/cm}^2$, the suggested values from hypothesis B agree with the measured G_{sh} -values, indicating that the Si melt destroys the SiO₂ and extends to the c-Si seed layer. Therefore, the Si melt recrystallizes into a single-crystal layer.

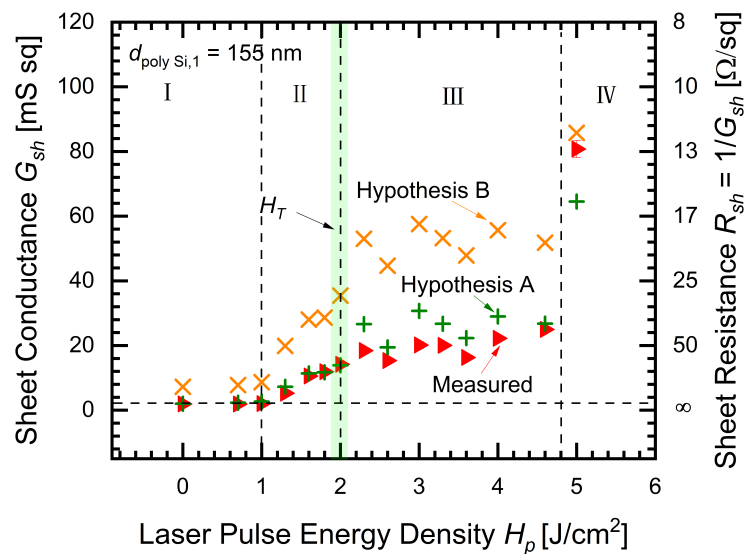


Figure 11. Comparison of the measured G_{sh} from layers including SiO_2 with the expected G_{sh} from hypothesis A and hypothesis B. For $H_p \leq 4.6 \text{ J/cm}^2$, where SiO_2 acts as a barrier against the Si melt, the measured G_{sh} -values agree well with hypothesis A, suggesting that the Si melt is recrystallized to an L-poly Si structure. However, for $H_p = 5 \text{ J/cm}^2$, the measured value agrees with hypothesis B, which implies that the Si melt destroys the SiO_2 and melts a part of a c-Si substrate. As a result, a mono-crystalline Si layer grows by liquid phase epitaxy.

Figure 12 summarizes the findings and illustrates the role of SiO_2 in a crystallization process. In the poly Si/ SiO_2 /c-Si structures, the SiO_2 separates a poly Si layer from a c-Si substrate and prevents the Si melt propagation to the c-Si bulk which acts as a seed layer. This results in a seedless crystallization of Si melt into an L-poly Si structure. However, for structures without SiO_2 and for structures where the SiO_2 is destroyed by excessive H_p , the Si melt reaches the c-Si substrate, and a mono-crystalline Si regrows by liquid phase epitaxy from the bottom c-Si substrate. The recrystallized single crystal structure has increased mobility and, hence, higher G_{sh} -values compared to structures where the Si melt recrystallizes to an L-poly Si structure.

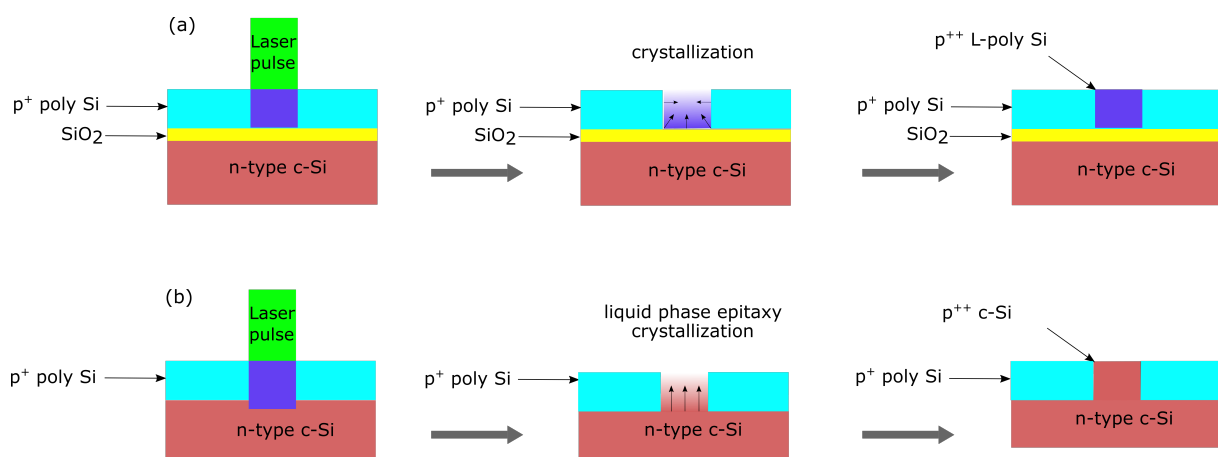


Figure 12. Role of SiO_2 in the crystallization mechanism of laser-activated samples. (a) A laser pulse with sufficient energy melts the poly Si layer, but the SiO_2 blocks the Si melt transfer to the c-Si bulk, resulting in the seedless crystallization of the Si melt into a laser-crystallized L-poly Si structure. (b) In the absence of an interfacial oxide, the Si melt propagates to the substrate and melts a portion of the c-Si bulk. After stopping the laser pulse, the molten Si recrystallizes by liquid phase epitaxy from the underlying c-Si substrate with the same lattice structure.

6. Passivation

We quantify the passivation quality of the fabricated lifetime samples (see Figure 2b) in terms of the implied open circuit voltage (iV_{OC}) and the saturation current density (J_0), which are derived from the QSSPC measurements using a Sinton WCT-120 tool.

Figure 13a compares the measured iV_{OC} of the samples with and without SiO_2 for a poly Si layer with $d_{\text{poly Si},1} = 155$ nm. For $H_p < 4.6$ J/cm², the majority of samples with SiO_2 show a good passivation quality with the highest $iV_{OC} = 721$ mV, which is comparable with the highest reported values for p⁺-poly Si/ SiO_2 passivation stacks [38,39]. The reason for the slight reduction in iV_{OC} for 2 J/cm² $< H_p < 2.6$ J/cm² is not clear and requires further scrutiny. Nearly 100 mV higher iV_{OC} is measured for most samples with SiO_2 compared to those without the SiO_2 . Such a high difference in a measured iV_{OC} is attributed to the double role of SiO_2 in the passivation quality. The SiO_2 in a poly Si/ SiO_2 /c-Si structure chemically passivates the dangling bonds on the c-Si surface. It simultaneously limits the dopant diffusion from the poly Si layer to the c-Si bulk and creates a large doping gradient at the interface, which leads to increased field-effect passivation and reduced Auger recombination. For $H_p = 4.6$ J/cm², the measured iV_{OC} of the samples with SiO_2 is reduced from $iV_{OC} = 720$ mV to $iV_{OC} = 661$ mV, which hints at damaged SiO_2 . Damage of the SiO_2 is also suggested by the increased depth of the doping profile for $H_p = 4.6$ J/cm² with respect to the lower laser pulse energy densities in Figure 4b. Increasing the used H_p to $H_p = 5$ J/cm² leads to further degradation of the passivation, resulting in a low $iV_{OC} = 624$ mV. This value matches the iV_{OC} values measured for samples without SiO_2 , which indicates a destroyed SiO_2 . This finding is also supported by the ECV profile in Figure 4b. The ECV profile of $H_p = 5$ J/cm² implies that the Si melt destroyed the SiO_2 and extended to the c-Si bulk.

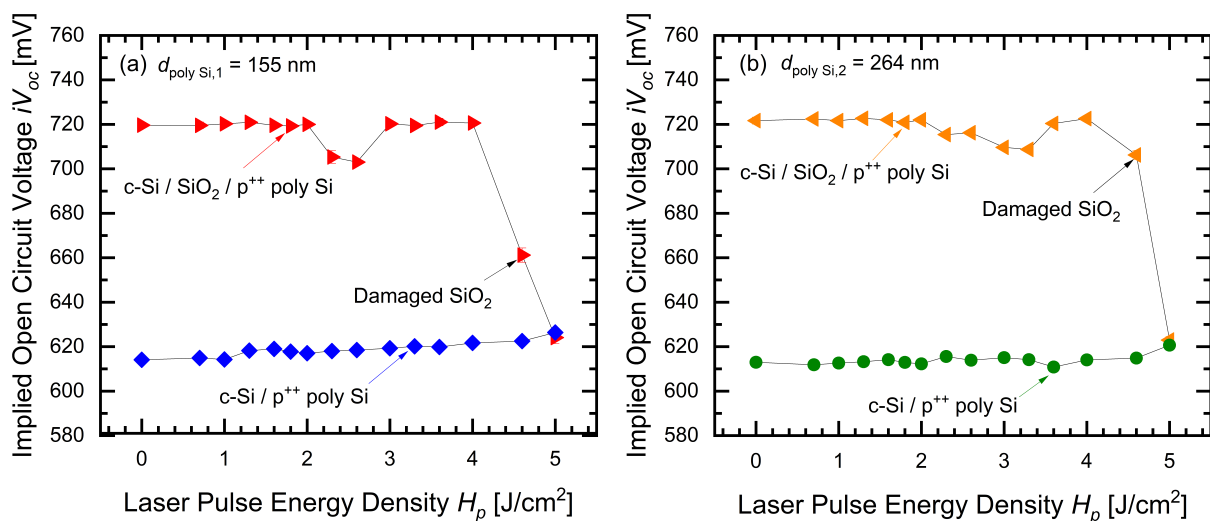


Figure 13. (a) Implied open circuit voltage iV_{OC} of samples with and without SiO_2 with a poly Si layer thickness $d_{\text{poly Si},1} = 155$ nm. For $H_p < 4.6$ J/cm² samples with SiO_2 mostly show high $iV_{OC} = 721$ mV. But, $H_p = 4.6$ J/cm² reduces the iV_{OC} by nearly 60 mV by damaging the SiO_2 . The $H_p = 5$ J/cm² destroys the SiO_2 and lowers the iV_{OC} to values comparable with samples without SiO_2 . (b) Increasing the tested poly Si thickness to $d_{\text{poly Si},2} = 264$ nm does not affect the passivation quality. For $H_p < 4.6$ J/cm², the majority of the samples show a good passivation quality with the highest $iV_{OC} = 722$ mV. However, a thicker poly Si layer reduces the damage caused by $H_p = 4.6$ J/cm² to the SiO_2 and results in higher iV_{OC} values compared to samples with a thinner poly Si layer. Still, $H_p = 5$ J/cm² destroys the SiO_2 and strongly reduces the iV_{OC} .

Figure 13b shows the measured iV_{OC} of samples with and without SiO_2 with a poly Si layer thickness $d_{\text{poly Si},2} = 264$ nm. The highest measured $iV_{OC} = 722$ mV is comparable

with the maximum measured iV_{OC} of samples with thinner poly Si layers, implying that the passivation quality does not significantly depend on the tested poly Si layer thickness. This behavior is expected and also supported by other studies of poly Si/SiO₂ passivation layers [34,41]. Similar to the samples with a thinner poly Si layer, in samples with a poly Si layer of $d_{\text{poly Si},2} = 264$ nm thickness, the presence of the SiO₂ leads to a higher iV_{OC} compared to samples without SiO₂ for $H_p < 4.6$ J/cm². However, the iV_{OC} loss for $H_p = 4.6$ J/cm² is less pronounced in samples with increased poly Si layer thickness compared to the samples with thinner poly Si layers. This is plausible since the increased poly Si layer reduces the damage from the Si melt to the SiO₂. Nevertheless, the same measured iV_{OC} of samples with and without SiO₂ shows that increasing the poly Si layer thickness from $d_{\text{poly Si},1} = 155$ nm to $d_{\text{poly Si},2} = 264$ nm does not prevent the SiO₂ destruction and the passivation loss for $H_p = 5$ J/cm².

Figure 14a,b shows the extracted saturation current densities J_0 of symmetrical passivation samples with SiO₂ from the effective lifetime (τ_{eff}) measurement. Due to the symmetry of the lifetime samples, we show $J_0/2$, representing a saturation current density per side. The J_0 values follow the trend of iV_{OC} shown in Figure 13a,b. For the H_p range, that does not damage the interfacial oxide ($H_p < 4.6$ J/cm²) samples with both poly Si layers $d_{\text{poly Si},1} = 155$ nm and $d_{\text{poly Si},2} = 264$ nm providing low J_0 , with the best sample achieving $J_0 = 6.7$ fA/cm². The $H_p = 4.6$ J/cm² damages the SiO₂ in samples with a thinner poly Si layer and sharply increases the saturation current density to $J_0 = 112$ fA/cm². In contrast, the increased poly Si thickness in the $d_{\text{poly Si},2} = 264$ nm structure reduces the damage caused by $H_p = 4.6$ J/cm² and provides only a moderately degraded passivation quality with $J_0 = 17$ fA/cm². The highest used $H_p = 5$ J/cm² destroys the SiO₂ for both poly Si thicknesses and results in $J_0 = 501$ fA/cm² and $J_0 = 482$ fA/cm² for $d_{\text{poly Si},1} = 155$ nm and $d_{\text{poly Si},2} = 264$ nm, respectively.

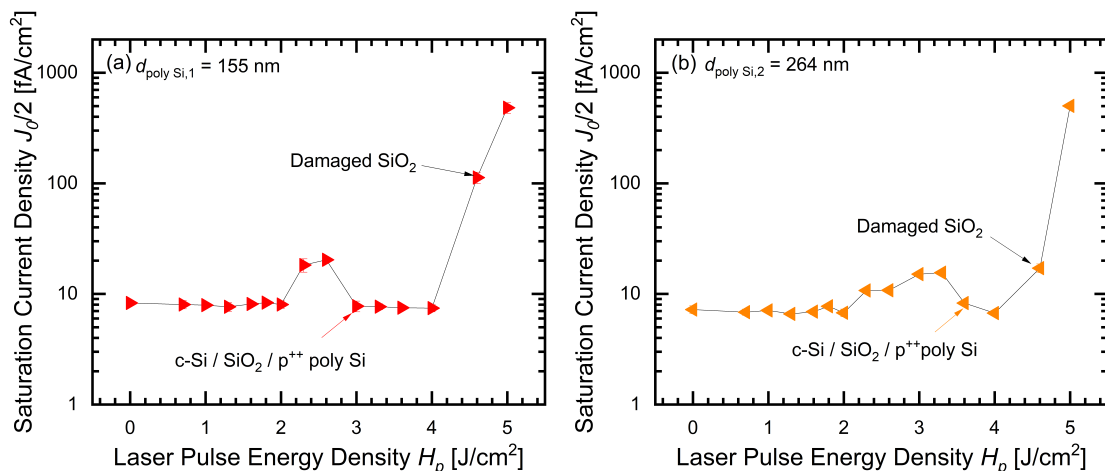


Figure 14. Saturation current densities J_0 per side of symmetrical lifetime samples with SiO₂. (a) A poly Si layer with $d_{\text{poly Si},1} = 155$ nm: For $H_p < 4.6$ J/cm² where the SiO₂ is not damaged, the majority of samples show good surface passivation with $J_0 < 10$ fA/cm². The $H_p = 4.6$ J/cm² leads to damaged SiO₂ and, consequently, a higher $J_0 = 112$ fA/cm². The $H_p = 5$ J/cm² destroys the SiO₂ and results in $J_0 = 482$ fA/cm². (b) A poly Si layer with $d_{\text{poly Si},2} = 264$ nm: Similar to the samples with a thinner poly Si layer, $H_p < 4.6$ J/cm² results in low J_0 , with the best sample achieving $J_0 = 6.7$ fA/cm². The increased thickness of the poly Si layer reduces the damage of the Si melt to the SiO₂ for $H_p = 4.6$ J/cm², which results in a lower $J_0 = 17$ fA/cm² compared to the samples with a thinner poly Si layer. The high measured J_0 for $H_p = 5$ J/cm² shows that increasing the thickness of the poly Si layer does not prevent the SiO₂ destruction with the highest H_p .

7. Summary

This work has shown the feasibility of a laser activation process for p⁺⁺-poly Si/SiO₂ passivation stacks. We tested various H_p in a wide range of 0.7 J/cm² $\leq H_p \leq 5$ J/cm² on

samples with two poly Si layer thicknesses of $d_{\text{poly Si},1} = 155$ nm and $d_{\text{poly Si},2} = 264$ nm. The poly Si layers already contain boron due to previous boron furnace diffusion. For both poly Si layers, the activation process begins when the laser pulse starts to melt the poly Si layer at the melting threshold laser pulse energy density $H_p \approx 1$ J/cm². For $H_p \geq 1$ J/cm², the melt depth of Si and, consequently, the dopant activation, linearly increases with increasing H_p . The activation process is completed when the H_p is high enough to melt the entire poly Si layer. Laser pulse energy densities $H_p = 2$ J/cm² and $H_p = 2.9$ J/cm² fully melt the $d_{\text{poly Si},1} = 155$ nm and $d_{\text{poly Si},2} = 264$ nm layers, respectively. The activation process becomes saturated for higher H_p up to $H_p = 4$ J/cm². Further increase in the H_p results in damaged or destroyed SiO₂ by the Si melt. The amount of damage induced by the high H_p depends on the poly Si layer thicknesses. The $H_p = 4.6$ J/cm² severely damages the $d_{\text{poly Si},1} = 155$ nm poly Si layer, while the damage is less pronounced for the samples with thicker poly Si layers. However, for both poly Si layers, the highest used $H_p = 5$ J/cm² destroys the SiO₂.

Further, we have investigated the recrystallization process after melting the poly Si layers with the laser process. The SiO₂ inhibits the transfer of the Si melt to the c-Si bulk up to $H_p = 4.6$ J/cm², resulting in seedless crystallization of the Si melt into a laser-crystallized L-poly Si structure. In the absence of SiO₂, and for structures where excessive H_p destroys the SiO₂, mono-crystalline Si grows by liquid phase epitaxy from the bottom c-Si bulk, which acts as a seed layer.

Additionally, the passivation study on the symmetrical lifetime samples shows that the passivation quality is independent of the thickness of the tested poly Si layers. The p⁺⁺-poly Si/SiO₂ structures with both poly Si layer thicknesses show a good passivation quality, with the best sample achieving $iV_{OC} = 722$ mV and $J_0 = 6.7$ fA/cm². Only samples processed with high $H_p = 4.6$ J/cm² show a degraded passivation quality due to the damaged SiO₂, especially for the samples with thinner poly Si layers where the damage to SiO₂ is more significant.

8. Conclusions

By choosing the appropriate laser pulse energy density, a green laser can be used to locally melt a poly Si layer in a poly Si/SiO₂ passivation stack, resulting in a high active boron concentration around $n \approx 5 \times 10^{20}$ cm⁻³ within the poly Si layers. After a high-temperature annealing step and capping with SiN_x:H, these laser-activated stacks achieve very high passivation quality with $iV_{OC} = 722$ mV and $J_0 = 6.7$ fA/cm². The achieved passivation quality shows that the interfacial SiO₂ layer is not destroyed during the laser process.

This work shows that high active boron concentrations is achieved in the laser-activated parts of poly Si layers. As described in ref. [15], high active boron concentrations in poly Si create the etch stop layer and result in the local p⁺⁺-poly Si/SiO₂ stacks after the etching process in an alkaline solution. In the future, we will use this maskless patterning method to create local p⁺⁺-poly Si/SiO₂ layers for the advanced passivated contact solar cells with p⁺⁺-poly Si/SiO₂ passivation stacks on the front side. In this cell structure, the p⁺⁺-poly Si/SiO₂ passivation stacks should be locally created under the front metal contacts to avoid parasitic absorption from the heavily doped poly Si layer.

One potential challenge is the observed reduction in high active boron concentration upon the high-temperature post-annealing step. Since solar cell production includes several high-temperature steps, like thermal diffusion, subsequent research in this regard is needed to maintain the high active boron concentration throughout the whole processing sequence.

Author Contributions: Conceptualization and experiment design, S.S.K., J.H. and J.H.W.; sample preparation, S.S.K.; measurements S.S.K.; modeling, S.S.K.; writing, S.S.K.; review and editing, J.H., R.Z.-G. and J.H.W.; supervision, J.H. and J.H.W.; data analysis and visualization, S.S.K.; project administration, J.H. All authors have read and agreed to the published version of the manuscript.

Funding: This research was funded by Bundesministerium für Wirtschaft und Klimaschutz (BMWK), funding reference: 03EE1138A.

Institutional Review Board Statement: Not applicable.

Informed Consent Statement: Not applicable.

Data Availability Statement: Not available.

Acknowledgments: This work was supported by the German Federal Ministry for Economic Affairs and Climate Action under contract number 03EE1138A (SelFi). The corresponding author also thanks the DAAD organization for the Ph.D. scholarship. A special thanks to Radovan Kopecek, managing director of ISC Konstanz, for organizing the corresponding author's transfer to ISC Konstanz. We would like to thank all colleagues at ISC Konstanz who helped with the sample preparation and processing, Mahdi Malekshahi from ipv Stuttgart for the XRD measurements, and acknowledge the support of Michael Saliba the director of ipv Stuttgart. We also thank Jan Lossen from ISC Konstanz for the valuable insights.

Conflicts of Interest: The authors declare no conflicts of interest.

References

- Kafle, B.; Goraya, B.S.; Mack, S.; Feldmann, F.; Nold, S.; Rentsch, J. TOPCon—Technology options for cost efficient industrial manufacturing. *Sol. Energy Mater. Sol. Cells* **2021**, *227*, 111100. [\[CrossRef\]](#)
- Glunz, S.; Steinhauser, B.; Polzin, J.I.; Luderer, C.; Grübel, B.; Niewelt, T.; Okasha, A.; Bories, M.; Nagel, H.; Krieg, K.; et al. Silicon-based passivating contacts: The TOPCon route. *Prog. Photovoltaics Res. Appl.* **2021**, *31*, 341–359. [\[CrossRef\]](#)
- Glunz, S.W.; Feldmann, F. SiO₂ surface passivation layers—A key technology for silicon solar cells. *Sol. Energy Mater. Sol. Cells* **2018**, *185*, 260–269. [\[CrossRef\]](#)
- Chen, Y.; Chen, D.; Liu, C.; Wang, Z.; Zou, Y.; He, Y.; Wang, Y.; Yuan, L.; Gong, J.; Lin, W.; et al. Mass production of industrial tunnel oxide passivated contacts (i-TOPCon) silicon solar cells with average efficiency over 23% and modules over 345 W. *Prog. Photovoltaics Res. Appl.* **2019**, *27*, 827–834. [\[CrossRef\]](#)
- Nandakumar, N.; Rodriguez, J.; Kluge, T.; Große, T.; Fondop, L.; Padhamnath, P.; Balaji, N.; König, M.; Duttgupta, S. Approaching 23% with large-area monoPoly cells using screen-printed and fired rear passivating contacts fabricated by inline PECVD. *Prog. Photovoltaics Res. Appl.* **2019**, *27*, 107–112. [\[CrossRef\]](#)
- Chaudhary, A.; Hoß, J.; Lossen, J.; Huster, F.; Kopecek, R.; van Swaaij, R.; Zeman, M. Screen Printed Fire-Through Contact Formation for Polysilicon-Passivated Contacts and Phosphorus-Diffused Contacts. *IEEE J. Photovoltaics* **2022**, *12*, 462–468. [\[CrossRef\]](#)
- Yang, G.; Guo, P.; Procel, P.; Limodio, G.; Weeber, A.; Isabella, O.; Zeman, M. High-efficiency black IBC c-Si solar cells with poly-Si as carrier-selective passivating contacts. *Sol. Energy Mater. Sol. Cells* **2018**, *186*. [\[CrossRef\]](#)
- Yuan, S.; Cui, Y.; Zhuang, Y.; Chen, P.; Hu, Y.; Yang, B.; Yu, Y.; Ren, Y.; Wang, W.; Chen, W.; et al. PERC Silicon Solar Cells with Front Polysilicon Passivating Contacted Selective Emitter. *Phys. Status Solidi (RRL) Rapid Res. Lett.* **2021**, *15*, 2100057. [\[CrossRef\]](#)
- Sze, S.; Lee, M. Semiconductor Devices: Physics and Technology. In *Semiconductor Devices, Physics and Technology*; Wiley: Hoboken, NJ, USA, 2012; p. 239.
- Trumbore, F.A. Solid solubilities of impurity elements in germanium and silicon. *Bell Syst. Tech. J.* **1960**, *39*, 205–233. [\[CrossRef\]](#)
- Padhamnath, P.; Nampalli, N.; Khanna, A.; Nagarajan, B.; Aberle, A.G.; Duttgupta, S. Progress with passivation and screen-printed metallization of Boron-doped monoPoly™ layers. *Solar Energy* **2022**, *231*, 8–26. [\[CrossRef\]](#)
- Carlsson, C.; Esturo-Bretón, A.; Ametowobla, M.; Köhler, J.; Werner, J. Laser doping for selective silicon solar cell emitter. In Proceedings of the 21st European Photovoltaic Solar Energy Conference, Dresden, Germany, 4–8 September 2006; pp. 938–940.
- Zhang, C.; Shen, H.; Sun, L.; Yang, J.; Wu, S.; Lu, Z. Bifacial p-Type PERC Solar Cell with Efficiency over 22% Using Laser Doped Selective Emitter. *Energies* **2020**, *13*, 1388. [\[CrossRef\]](#)
- Zapf-Gottwick, R.; Seren, S.; Fernandez-Robledo, S.; Wete, E.P.; Schiliro, M.; Hassan, M.; Mihailetchi, V.; Buck, T.; Kopecek, R.; Köhler, J.; et al. Solar Cells with Laser Doped Boron Layers from Atmospheric Pressure Chemical Vapor Deposition. *Solar* **2022**, *2*, 274–292. [\[CrossRef\]](#)
- Buchholz, F.; Linke, J.; Hoß, J.; Chu, H.; Mihailetchi, V.; Chaudhary, A.; Arumughan, J.; Lossen, J.; Kopecek, R.; Wefringhaus, E. Local Passivating Contacts from Laser Doped P+ Polysilicon. In Proceedings of the 38th European Photovoltaic Solar Energy Conference and Exhibition, Online, 6–10 September 2021; pp. 140–143. [\[CrossRef\]](#)
- Feldmann, F.; Nicolai, M.; Müller, R.; Reichel, C.; Hermle, M. Optical and electrical characterization of poly-Si/SiO_x contacts and their implications on solar cell design. *Energy Procedia* **2017**, *124*, 31–37. In Proceedings of the 7th International Conference on Silicon Photovoltaics, SiliconPV 2017, Freiburg, Germany, 3–5 April 2017.
- Feldmann, F.; Reichel, C.; Müller, R.; Hermle, M. The application of poly-Si/SiO_x contacts as passivated top/rear contacts in Si solar cells. *Sol. Energy Mater. Sol. Cells* **2017**, *159*, 265–271. [\[CrossRef\]](#)
- Haase, F.; Hollemann, C.; Schäfer, S.; Merkle, A.; Rienäcker, M.; Krügener, J.; Brendel, R.; Peibst, R. Laser contact openings for local poly-Si-metal contacts enabling 26.1. *Sol. Energy Mater. Sol. Cells* **2018**, *186*, 184–193. [\[CrossRef\]](#)

19. Chen, K.; Napolitani, E.; De Tullio, M.; Jiang, C.S.; Guthrey, H.; Sgarbossa, F.; Theingi, S.; Nemeth, W.; Page, M.; Stradins, P.; et al. Pulsed Laser Annealed Ga Hyperdoped Poly-Si/SiO_x Passivating Contacts for High-Efficiency Monocrystalline Si Solar Cells. *Energy Environ. Mater.* **2023**, *6*, e12542. [CrossRef]
20. Hassan, M.; Dahlinger, M.; Köhler, J.R.; Zapf-Gottwick, R.; Werner, J.H. Unified Model for Laser Doping of Silicon from Precursors. *Materials* **2021**, *14*, 2322. [CrossRef]
21. Sinton, R.A.; Cuevas, A.; Stuckings, M. Quasi-steady-state photoconductance, a new method for solar cell material and device characterization. In Proceedings of the Conference Record of the Twenty Fifth IEEE Photovoltaic Specialists Conference—1996, Washington, DC, USA, 13–17 May 1996; pp. 457–460.
22. Kamins, T., Dopant Diffusion and Segregation. In *Polycrystalline Silicon for Integrated Circuit Applications*; Springer US: Boston, MA, USA, 1988; pp. 91–123. [CrossRef]
23. Kodera, H. Diffusion Coefficients of Impurities in Silicon Melt. *Jpn. J. Appl. Phys.* **1963**, *2*, 212. [CrossRef]
24. Vick, G.L.; Whittle, K.M. Solid Solubility and Diffusion Coefficients of Boron in Silicon. *J. Electrochem. Soc.* **1969**, *116*, 1142. [CrossRef]
40. Poate, J.M.; Brown, W.L. Laser annealing of silicon. *Phys. Today* **1982**, *35*, 24–30. [CrossRef]
40. White, C.W.; Wilson, S.R.; Appleton, B.R.; Young, F.W. Supersaturated substitutional alloys formed by ion implantation and pulsed laser annealing of group-III and group-V dopants in silicon. *J. Appl. Phys.* **1980**, *51*, 738–749. [CrossRef]
27. Fiory, A.; Bourdelle, K.K. A comparative study of laser and thermal annealing of boron-implanted silicon. *J. Appl. Phys.* **1978**, *49*, 3912–3917. [CrossRef]
28. Lim, S.; Williams, J. Electrical and Optical Doping of Silicon by Pulsed-Laser Melting. *Micro* **2021**, *2*, 1–22. [CrossRef]
29. Goetzlich, J.; Tsien, P.; Ryssel, H. Relaxation Behavior of Metastable As and P Concentrations in Si After Pulsed and CW Laser Annealing. *MRS Online Proc. Libr. (OPL)* **1983**, *23*, 235. [CrossRef]
30. Esturo-Breton, A.; Ametowobla, M.; Köhler, J.; Werner, J. *Laser Doping for Crystalline Silicon Solar Cell Emitters*; European Photovoltaic Solar Energy Conference, 20: München, Germany, 2005; pp. 851–854.
31. McConnell, A.; Uma, S.; Goodson, K. Thermal Conductivity of Doped Polysilicon Layers. *Microelectromechanical Syst.* **2001**, *10*, 360–369. [CrossRef]
32. Haynes, W.M., Thermal Conductivity of Metals and Semiconductors as a Function of Temperature. In *CRC Handbook of Chemistry and Physics*; CRC: Boca Raton, FL, USA, 2014; pp. 212–221.
37. Seto, J.Y.W. The electrical properties of polycrystalline silicon films. *J. Appl. Phys.* **1975**, *46*, 5247–5254. [CrossRef]
34. Çiftçinar, H.E.; Stodolny, M.K.; Wu, Y.; Janssen, G.J.; Löffler, J.; Schmitz, J.; Lenes, M.; Luchies, J.M.; Geerligs, L. Study of screen printed metallization for polysilicon based passivating contacts. *Energy Procedia* **2017**, *124*, 851–861. In Proceedings of the 7th International Conference on Silicon Photovoltaics, SiliconPV 2017, Freiburg, Germany, 3–5 April 2017. [CrossRef]
35. Masetti, G.; Severi, M.; Solmi, S. Modeling of carrier mobility against carrier concentration in arsenic-, phosphorus-, and boron-doped silicon. *IEEE Trans. Electron Devices* **1983**, *30*, 764–769. [CrossRef]
36. Sheet Resistance Calculator. Available online: <https://www2.pvlighthouse.com.au/calculators/sheet> (accessed on 20 December 2022).
37. Chong, Y.F.; Pey, K.L.; Lu, Y.F.; Wee, A.T.S.; Osipowicz, T.; Seng, H.L.; See, A.; Dai, J.Y. Liquid-phase epitaxial growth of amorphous silicon during laser annealing of ultrashallow p+/n junctions. *Appl. Phys. Lett.* **2000**, *77*, 2994–2996. [CrossRef]
38. Ma, D.; Liu, W.; Xiao, M.; Yang, Z.; Liu, Z.; Liao, M.; Han, Q.; Cheng, H.; Xing, H.; Ding, Z.; et al. Highly improved passivation of PECVD p-type TOPCon by suppressing plasma-oxidation ion-bombardment-induced damages. *Solar Energy* **2022**, *242*, 1–9. [CrossRef]
39. Stuckelberger, J.; Yan, D.; Phang, S.P.; Samundsett, C.; Wang, J.; Antognini, L.; Haug, F.J.; Wang, Z.; Yang, J.; Zheng, P.; et al. Pre-annealing for improved LPCVD deposited boron-doped poly-Si hole-selective contacts. *Solar Energy Mater. Sol. Cells* **2023**, *251*, 112123. [CrossRef]
40. Chaudhary, A.; Hoß, J.; Lossen, J.; Huster, F.; Kopecek, R.; van Swaaij, R.; Zeman, M. Influence of Polysilicon Thickness on Properties of Screen-Printed Silver Paste Metallized Silicon Oxide/Polysilicon Passivated Contacts. *Phys. Status Solidi (a)* **2021**, *218*, 2100243. [CrossRef]
41. Padhamnath, P.; Buatis, J.K.; Khanna, A.; Nampalli, N.; Nandakumar, N.; Shanmugam, V.; Aberle, A.G.; Duttgupta, S. Characterization of screen printed and fire-through contacts on LPCVD based passivating contacts in monoPoly™ solar cells. *Solar Energy* **2020**, *202*, 73–79. [CrossRef]

Disclaimer/Publisher's Note: The statements, opinions and data contained in all publications are solely those of the individual author(s) and contributor(s) and not of MDPI and/or the editor(s). MDPI and/or the editor(s) disclaim responsibility for any injury to people or property resulting from any ideas, methods, instructions or products referred to in the content.